The Pennsylvania State University

The Graduate School

MULT-SCALE MODELLING AND COMPUTATIONAL FLUID DYNAMICS ANALSYIS OF TRANSITION METAL DICHALCOGENIDE (TMD) GROWTH IN AN MOCVD CHAMBER

A Thesis in

Mechanical Engineering

by

Suhaib Zafar

Submitted in Partial Fulfillment
of the Requirements
for the Degree of

Master of Science

December 2020

The thesis of Suhaib Zafar was reviewed and approved by the following:

Yuan Xuan
Associate Professor of Mechanical Engineering
Thesis Adviser

Robert F. Kunz
Professor of Mechanical Engineering

Karen A. Thole
Department Head of Mechanical Engineering and Distinguished Professor

ABSTRACT

Among semiconductors, Transition Metal Dichalcogenides (TMDs) are a promising new type, offering exciting new possibilities in applications such as light-emitting diodes. A variety of synthesis technologies for TMDs have been reported, foremost of which is the Metal Organic Chemical Vapor Deposition (MOCVD) method. Recently, researchers have applied MOCVD to synthesis of tungsten diselenide (WSe_2), which falls under the class of TMDs. To gain a better understanding of WSe_2 growth kinetics, researchers have experimented with different substrates, precursors, and various ranges of growth parameters such as temperature and pressure. It is crucial to gain this insight to benefit from its useful properties. Computational Fluid Dynamics (CFD) is a useful complement to experimentation in this regard, and in general is cheaper and faster. However, CFD simulations require a chemical kinetics model to be incorporated with heat transfer and fluid mechanics for it to be a useful analysis and prediction tool. Such models have been developed for other materials such as GaN and have proved useful in analyzing and optimizing growth of semiconductors. In a similar fashion, this thesis presents the use of CFD to analyze the impact of varying process parameters on WSe_2 growth in an MOCVD reactor used by researchers at the Penn State 2DCC facility. We utilized a gas-phase chemical kinetics model developed using a multi-scale modeling framework incorporating Density Functional Theory (DFT) and reactive molecular dynamics, presented in a previous study. A comparison of WSe_2 and $MoSe_2$ growth kinetics is also done in this context, highlighting key similarities as well as differences. Finally, based on the analysis of results obtained from varying process parameters, the effect of chamber geometry on WSe_2 growth was also analyzed using numerical experiments.

TABLE OF CONTENTS

LIST OF FIGURES

LIST OF TABLES

ACKNOWLEDGEMENTS

The author acknowledges the primary financial support of the National Science Foundation (NSF) through the Penn State 2D Crystal Consortium Materials Innovation Platform (2DCC-MIP) under NSF cooperative agreement no. DMR-1539916. This research was conducted with the Roar supercomputer computational resources provided by the Institute for Computational and Data Sciences (ICDS) at the Pennsylvania State University. Any opinions, findings, and conclusions or recommendations expressed in this publication are those of the author and do not necessarily reflect the views of the National Science Foundation (NSF).

Chapter 1.

Analysis of WSe_2 growth under different operating conditions

1.1 Introduction

In the ever-expanding research field of 2D materials, atomically thin Transition Metal Dichalcogenides (TMDs) are a novel and emerging class of semiconductors, exhibiting unique electrical and optical properties. A few examples include tunable band gaps (~1–2 eV) [1,2], spin valley coupling [3,4] and large exciton binding energy [5], allowing for a wide variety of applications such as solar cells, light-emitting diodes and phototransistors [6–8]. A TMD consists of one transition metal (M) and two chalcogen atoms (X). The focus of this article is tungsten diselenide (WSe_2), a semiconducting TMD that exhibits unique optical properties such as photoluminescence in its monolayer form [9].

A variety of synthesis technologies for TMDs including WSe_2 have been reported in literature. These include examples such as mechanical exfoliation [10,11], powder vaporization [12,13], and chemical vapor deposition (CVD) [14,15]. Mechanical exfoliation produces high quality monolayers of TMDs but suffers from the drawback of not being scalable [16,17]. CVD is an alternative to circumvent the impediment of scalability [18], however a major disadvantage of this technique is the difficulty of realizing uniform growth over large substrate areas [19]. Additionally, it is difficult to control and modulate the source supply in this method [20]. To circumvent these problems, the use of Metal-Organic Chemical Vapor Deposition (MOCVD) technique is desirable. Eichfeld et al. [21] reported the first such study for the synthesis of WSe_2, using a variety of substrates including sapphire and graphene. They emphasize the flexibility this technique offers in the gas-phase precursor selection and provide evidence that the MOCVD-grown WSe_2 is of superior quality to that of exfoliated heterostructures. Kang et al. [22] used MOCVD to grow 4-inch wafer-scale films of monolayer molybdenum disulphide (MoS_2) and its tungsten counterpart WS_2, reporting excellent spatial homogeneity.

Despite recent advancements in WSe_2 synthesis, however, its growth mechanisms are not very well-understood, and it is relatively much less studied than other TMDs, such as MoS_2. It is also known that WSe_2 is relatively difficult to synthesize, due to the lower reactivity of selenium precursors [23]. Additionally, experimental researchers are interested in studying how growth kinetics vary with different parameters such as substrate temperature and precursor flow rates [24]. For instance, Eichfeld et al. [21] analyze how temperature, total pressure, precursor flow rate ratios and total flow through the system have an impact on domain size, shape, and nucleation density. They quantify sensitivity of domain size to increasing temperature, pressure, and total flow rate, and suggest that there is an ideal Se:W ratio of 20,000 for domain growth. In a similar fashion, Zhou et al. [25] report WSe_2 domain size and nucleation density at various substrate temperatures and flow rates of carrier gas (argon). The authors conclude that higher growth temperature increases domain size and increasing flow rate of the carrier gas results in an increased domain density. The role of growth temperature on domain size and density is also discussed in another study by Eichfeld et al. [26] that incorporates a low-temperature nucleation step in WSe_2 synthesis.

It is therefore evident from these studies that optimizing growth parameters is crucial to realize the full benefit of the highly useful properties of WSe_2.

The Computational Fluid Dynamics (CFD) approach complements experiments to study semiconductor material synthesis, since it allows access to a wider range of process parameters for testing, with a lower cost to setup and run a numerical simulation [27]. Additionally, it can offer quantitative insight into the underlying physiochemical processes underway in the reactor during growth [28]. Such simulations, however, require a consideration of heat transfer and fluid mechanics coupled with detailed chemical kinetics models grounded in fundamental principles to predict MOCVD reactor behavior under different operating conditions [29]. These models can also be employed to provide optimal reactor designs for a given MOCVD process [30]. Previously, researchers have developed and used such models to analyze and optimize the growth of semiconductor materials such as ZnO and GaN [31,32]. For WSe_2 growth using MOCVD, however, the growth kinetics are not well-understood, as outlined earlier. To address this issue, the authors [33] developed a gas-phase chemical kinetics model utilizing a multi-scale modelling framework that incorporates Density Functional Theory (DFT) and the ReaxFF [34] reactive force field approach. This kinetics model was employed to run CFD simulations of the custom-designed MOCVD reactor used by researchers at the Penn State 2D Crystal Consortium (2DCC) facility. The results obtained from simulations showed good agreement with experiments, hence well-suited for the current work.

The aim of this study is to analyze the impact of varying operating conditions of the given reactor on WSe_2 crystal growth. To this end, a series of simulations were run, each of which varies a given process parameter, while holding others constant at a specified threshold. The four process parameters are growth temperature, chamber pressure, precursor injection method and H_2Se gas-phase precursor flow rate. The focus output is the gas-phase $W(SeH)_2Se_2$ concentration yield and its distribution over the growth substrate. This is because it represents the thermodynamic endpoint in the chemical model, analogous to WSe_2 in the experiments. The variation in this output is analyzed and discussed in terms of the underlying mechanisms, by applying principles from fluid mechanics and chemical kinetics.

1.2 Experimental Setup

This section provides a brief description of the MOCVD set-up used by experimental researchers at the 2D Crystal Consortium (2DCC) facility at Penn State for WSe_2 growth, along with test conditions for the baseline version. For a more detailed version on the MOCVD reactor, please refer to [33].

1.2.1 MOCVD chamber

The MOCVD system used for WSe_2 synthesis is custom-designed, consisting of a gas panel for precursors and gas sources (EMCORE), a cold-wall horizontal quartz tube reactor (CVD Equipment Corporation), a rotary vane pump and associated pressure control equipment, and an EGC-405 exhaust conditioning system for process exhaust abatement. The substrate is placed on a graphite rotating disc, housed in a rectangular susceptor. To achieve the desired growth temperature, RF induction coils are utilized. There are two separate T-shaped quartz injectors that

introduce the gas-phase precursors into the reactor. Both injectors have equidistant holes, each 1.27 mm in diameter. These holes abet distribution of the source gases over the entire wafer. There is an additional inlet for hydrogen, which serves as the background gas. A schematic of the set-up is shown in Figure 1.1(a).

1.2.2 Baseline test conditions

Hydrogen carrier gas is introduced at a 1000 sccm through both injector tubes along with precursors to ensure their delivery to the growth zone. An additional background flow of H_2 is maintained at 2500 sccm. The lower injector carries the transition metal precursor/hydrogen gas mixture while the upper injector carries the chalcogen precursor/hydrogen gas mixture. The flow rate of the transition metal precursor $W(CO)_6$ is 5.4×10^{-4} sccm. The chalcogen precursor H_2Se flow rate is maintained at 15 sccm. The growth temperature is 850°C, whereas pressure in the chamber is maintained at 200 Torr.

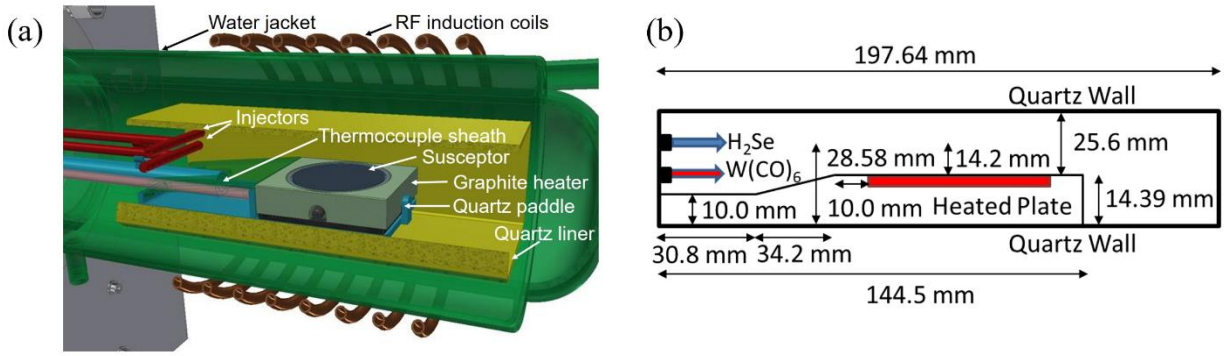

Figure 1.1 (a) Schematic of the MOCVD chamber used for WSe_2 growth (b) Schematic of the computational domain with key dimensions in mm

1.3 Numerical modeling and computational domain

1.3.1 Chemical kinetic model

The use of ReaxFF in conjunction with DFT results in a chemical model that contains 57 species and 162 reactions (forward and backward counted separately), with their corresponding activation energies (E_a). The procedure to compute activation energies is discussed in detail in a previous study reported by the authors [33]. CFD simulations require the use of modeling rate of reaction, which is achieved by utilizing the Arrhenius formulation: $k = Ae^{-\frac{E_a}{RT}}$

While the activation energies are known as outlined above, the pre-exponential factor A for each reaction is unknown. For unimolecular reactions, estimates for A are obtained by utilizing the Lindemann model with the Hinshelwood correction applied [35]. Owing to the low-pressure limit (applicable to MOCVD conditions), unimolecular reactions are treated as second-order, with hydrogen acting as the third-body collider. Bimolecular reactions, therefore, are treated as third-order, by utilizing a three-step mechanism that models this type, analogous to the Lindemann model [35]. Since bimolecular reactions are now third-order, the rate law for a reaction of the form $A + B \rightarrow C$ is a function of [A], [B] and a third body collider [M], where [M] = [H_2], as noted in

the discussion above on unimolecular reactions. Further details on computation of A factors can be found in [33].

1.3.2 Numerical modelling

An in-house flow solver NGA [36] was utilized for full-scale MOCVD chamber simulations. NGA solves the unsteady Navier-Stokes equations using a low Mach number assumption along with the species mass fraction and heat transport equations. The density of the gas-phase mixture is computed using the ideal gas law. Scalar discretization uses the BQUICK scheme, which ensures that the physical bounds of appropriate quantities are numerically preserved throughout the simulation. A computationally efficient, semi-implicit iterative method is used for the time-integration of chemical source terms for the transport equations of gas-phase species. This method has been shown to be free of lagging errors [37], and used successfully in reacting flow simulations, particularly in combustion applications for both laminar [38] and turbulent flows [39]. The time-step determined to be adequate for resolving chemical kinetics and transport processes was 5e−6. This value was used for all numerical experiments except when a deviation was required or helpful (in terms of reduction in the number of computational hours).

1.3.3 Computational Domain

The gas-phase precursor injection velocities were calculated using the experimental inlet conditions as described in Section 1.2.2. Based on the computed velocities, which are about 0.8 m/s at the injectors, the flow in the MOCVD chamber was determined to be laminar everywhere, based on a Reynolds number of about 2 at each injector, hence flow variation in the cross-stream is assumed to be negligible. Thus, a 2D computational domain was constructed with a domain length of 197.6 mm (including a part of the exhaust nozzle) and a domain height of 40.0 mm (including the upper and lower quartz walls), as shown in Fig. 1.1(b). A Cartesian grid with 358 points horizontally and 303 points vertically was used to spatially resolve the gas-phase chemical and transport processes. The grid is uniform in the vertical direction, but non-uniform in the horizontal direction beyond the graphite susceptor. A grid convergence study was conducted to verify that the current domain is adequate for spatial resolution of transport and chemical processes. For this purpose, a refined grid was constructed which is twice as finer as the original grid, but only where chemical reactions are expected to occur i.e. above the heated graphite plate. The refined grid has 518 points horizontally but uses 303 points vertically as before. A numerical experiment was then run with both grids, with the plate temperature at 923 K so that a greater time-step could be used, and the experiments can be conducted faster. The concentration yield of the species $W(SeH)_2Se_2$ above the graphite plate is plotted in Fig. 1.2 for the standard and the refined grid. The difference in yield between the standard and the finer grid for $W(SeH)_2Se_2$ is found to be 0.045% which implies that the use of the standard configuration (as described in this paragraph) is justified thanks to the immense savings in computational resources it offers.

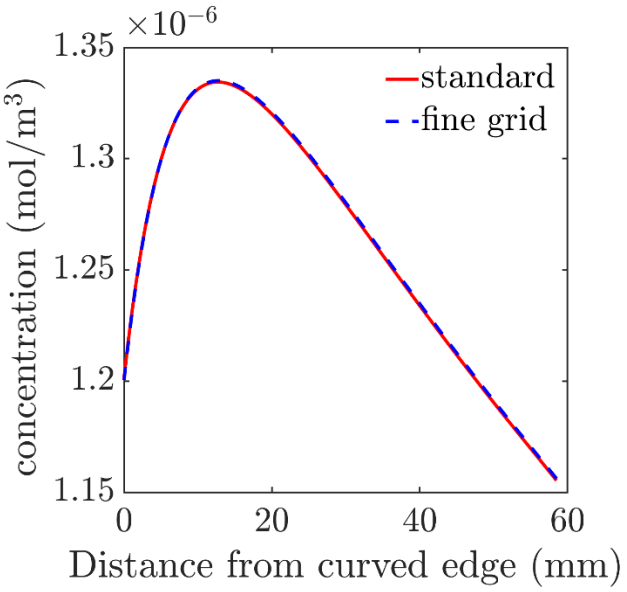

Figure 1.2 Concentration of $W(SeH)_2Se_2$ over the heated graphite plate (standard vs fine grid)

1.3.4 Variation in process parameters

As outlined in the introduction section, each of the four process parameters, namely, growth temperature, chamber pressure, precursor injection method and H_2Se gas-phase precursor flow rate were varied independently. The total flow rate for both injectors and the background flow were fixed at 1000 and 2500 sccm, respectively, for all runs. The test case A3 is the baseline (described in Section 1.2.2), thus highlighted in **bold**. The values for this case, as well as the testing range for all process parameters shown in Table 1, were provided by experimental researchers at the Penn State 2DCC facility.

Test Case	Temperature (°C)	Pressure (Torr)	Precursor injection method	H_2Se flow rate (sccm)
A1	650	200	Standard	15
A2	750	200	Standard	15
A3	850	200	Standard	15
A4	950	200	Standard	15
B1	850	50	Standard	15
B2	850	100	Standard	15
C1	850	200	Flipped	15
C2	850	200	Premixed	15
D1	850	200	Standard	5
D2	850	200	Standard	30
D3	850	200	Standard	50

Table 1 Test matrix for CFD simulations of WSe_2 growth

The fourth column in Table 1 lists the type of precursor injection method. The injection is termed **standard** when the transition metal precursor $W(CO)_6$ is injected via the lower injector, and the chalcogen precursor H_2Se via the upper injector (see Section 1.2.2). The **flipped** injection is simply the reversal of the standard injection, as the name suggests. Lastly, the injection is called **premixed** when both injectors are fed a mixture of hydrogen gas with the transition metal and chalcogen precursor. The flow rate for both precursors at each injector is half of its standard value, stated in Section 1.2.2.

1.4 Results and Discussion

1.4.1 Impact of varying growth temperature

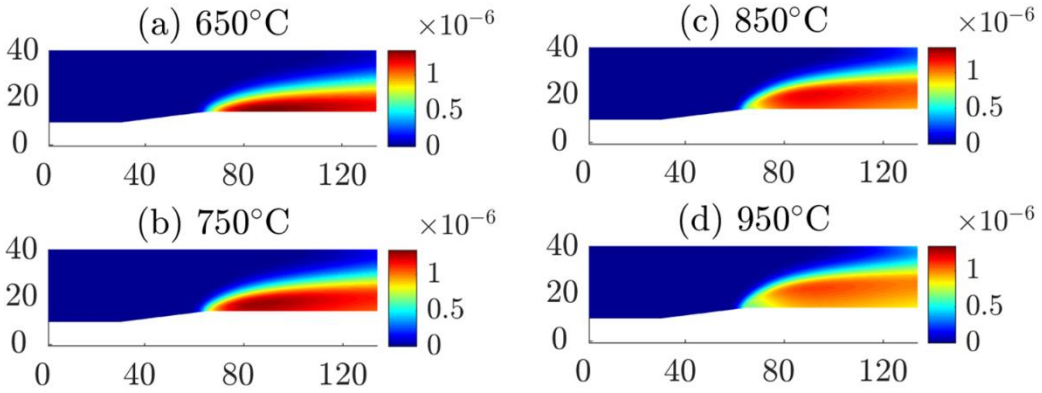

Figure 1.3 (a–d) 2D concentration plots for $W(SeH)_2Se_2$ at different growth temperatures

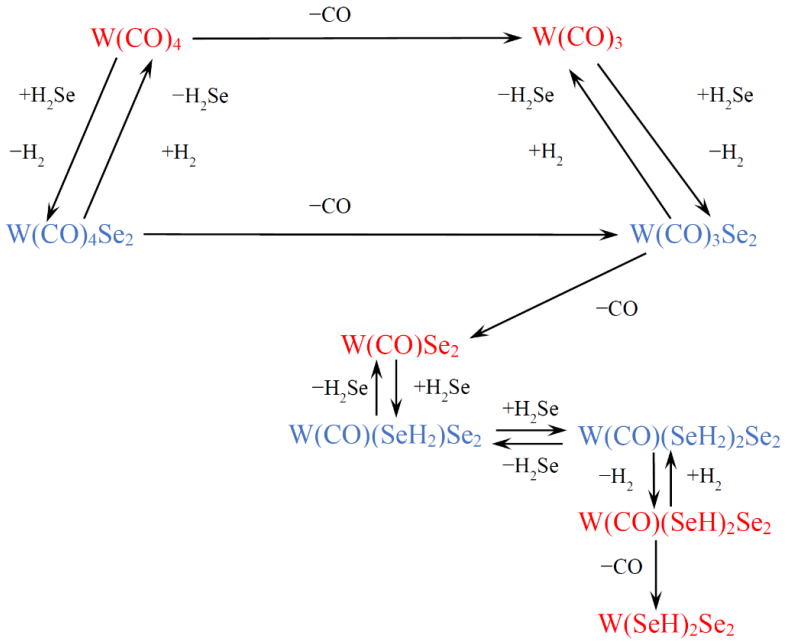

Figure 1.4 Reaction Graph showing major species in red

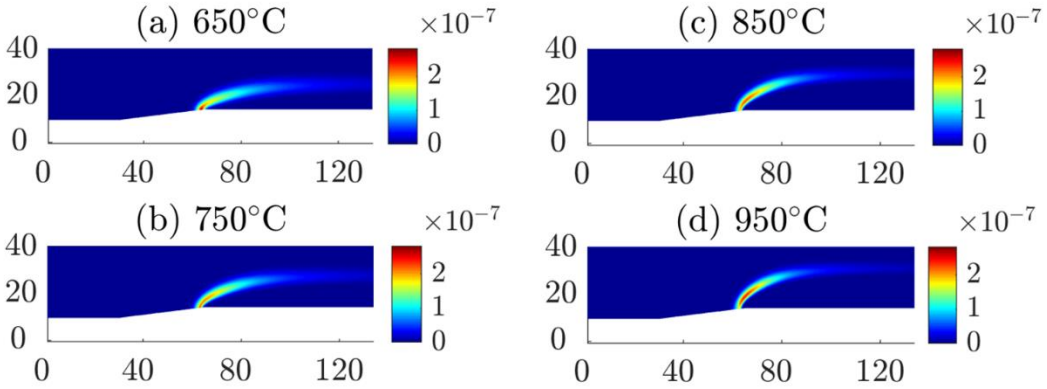

Figure 1.5 (a–d) 2D concentration plots for $W(CO)_4$ at different growth temperatures

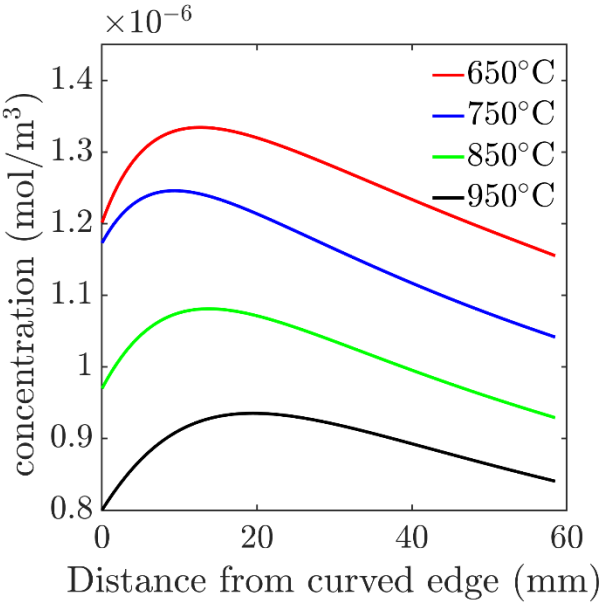

Figure 1.6 Concentration of $W(SeH)_2Se_2$ over the heated graphite plate

Fig. 1.3(a–d) shows the spatial distribution of $W(SeH)_2Se_2$ concentration for four different growth temperatures (cases A1–4 in Table 1). The inception point, found at the start of the graphite block, does not vary with changes in temperature. Additionally, the vertical spread of this species in the chamber increases with an increase in growth temperature. This can be explained by utilizing the Reaction Graph in Fig. 1.4 which delineates the pathway from the earliest species to the final product species $W(SeH)_2Se_2$. The pathway is composed of both one and two-way reactions, that involve the addition and loss of H_2Se and H_2, as well as CO abstraction reactions. The species shown in blue are low in concentration and merely act as a conduit in the chemical pathway. As can be observed in the graph, the species $W(CO)Se_2$ plays a crucial role in the formation of $W(SeH)_2Se_2$ since all major pathways from the reactants converge onto this species, which acts as a pivot in the chemical kinetics underway in the MOCVD reactor. From the observed connection in the reaction graph, it is inferred that the distribution of $W(SeH)_2Se_2$ as shown in Fig. 1.3(a–d)

follows that of an earlier species in the pathway, such as $W(CO)_4$. Indeed, this can be observed in Fig. 1.5(a–d) which shows the spatial distribution of $W(CO)_4$ concentration in the MOCVD reactor. For $W(CO)_4$, the location of its formation on the graphite block is upstream of that of $W(SeH)_2Se_2$, which is as expected, as it forms earlier in the pathway. The vertical spread of $W(CO)_4$ can also be observed to increase with an increase in growth temperature, similar for $W(SeH)_2Se_2$ as stated earlier.

Fig. 1.6 shows the concentration yield of $W(SeH)_2Se_2$ above the graphite plate. With an increase in temperature from 650°C to 950°C, a successive decrease in yield is observed. The decrease in yield is about 10–15% for each successive temperature increase. The distribution of $W(SeH)_2Se_2$ shows a peak in the range of 10–20 mm from the curved edge for each case, decreasing thereafter. For all cases of growth temperature, there is a shift in the peak of the distribution of no more than 5 mm. The decrease in $W(SeH)_2Se_2$ concentration yield atop the graphite plate can be explained by considering the effects of temperature on mixture density and a shift in chemical equilibrium of the reactions leading from $W(CO)Se_2$ to $W(SeH)_2Se_2$. The concentration of a gas-phase species is proportional to the density of the mixture, which decreases with an increase in temperature following the ideal gas law. Concurrently, the increase in temperature affects the H_2Se loss reactions in pathway from $W(CO)Se_2$ to $W(SeH)_2Se_2$, which have an activation energy in the range of 60–70 kJ/mol. Since the forward reactions have no barrier, the equilibrium constant κ dramatically reduces in magnitude with an increase in growth temperature. This decrease is less pronounced for the reactions involving H_2 addition and loss since both pathways have a barrier. This shift in the chemical equilibrium in conjunction with a decrease in mixture density leads to a lower concentration yield of $W(SeH)_2Se_2$.

1.4.2 Impact of varying chamber pressure

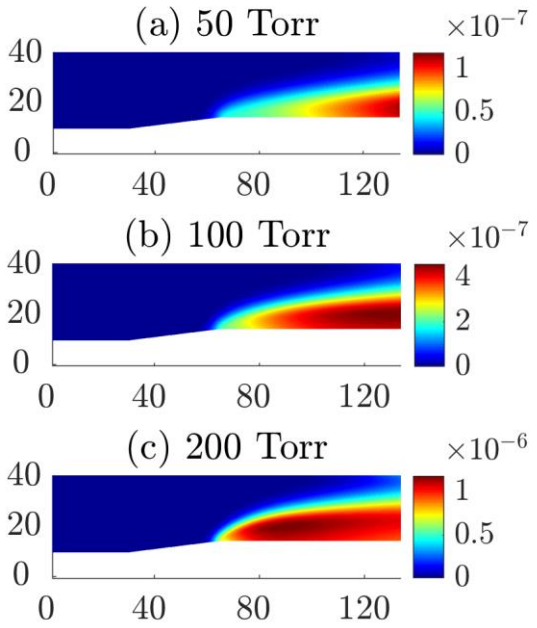

Figure 1.7 (a–c) 2D concentration plots for $W(SeH)_2Se_2$ at different chamber pressures

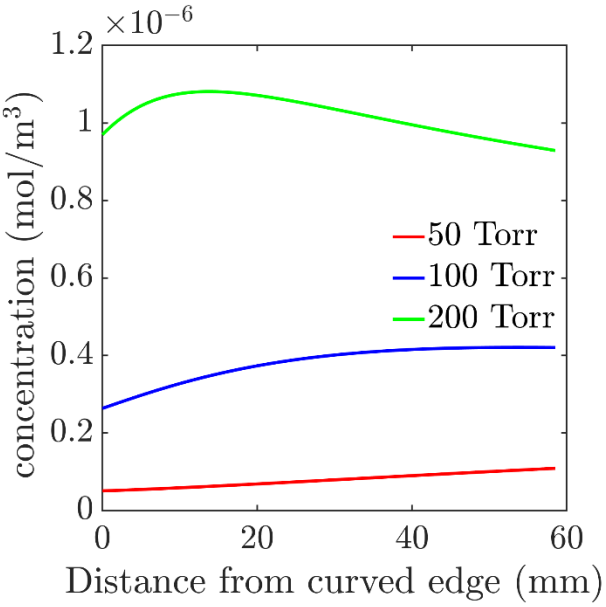

Figure 1.8 Concentration of $W(SeH)_2Se_2$ over the heated graphite plate

Fig. 1.7(a–c) shows the spatial distribution of $W(SeH)_2Se_2$ concentration for cases B1–2 and A3 (Table 1), ranging from 50–200 Torr of chamber pressure. The inception point, at the leading edge of the graphite block, does not seem to vary with changes in pressure. Similarly, the vertical spread of this species concentration is also found to be relatively insensitive to pressure variation. This is because the formation of this species is temperature-controlled. As shown in Fig. 1.8, an increase in pressure from 50 to 100 Torr results in a fourfold increase in the concentration of $W(SeH)_2Se_2$ over the plate. Doubling the pressure to 200 Torr causes a further increase in the concentration by a factor of three. Fig. 1.8 also shows the distribution of $W(SeH)_2Se_2$ atop the plate increasing monotonically at 50 Torr. At a pressure of 100 Torr however, a monotonic increase up to 40 mm followed by a plateau is observed. When the pressure is further increased to 200 Torr, a peak in distribution is found at about 15 mm, and decreases beyond 20 mm.

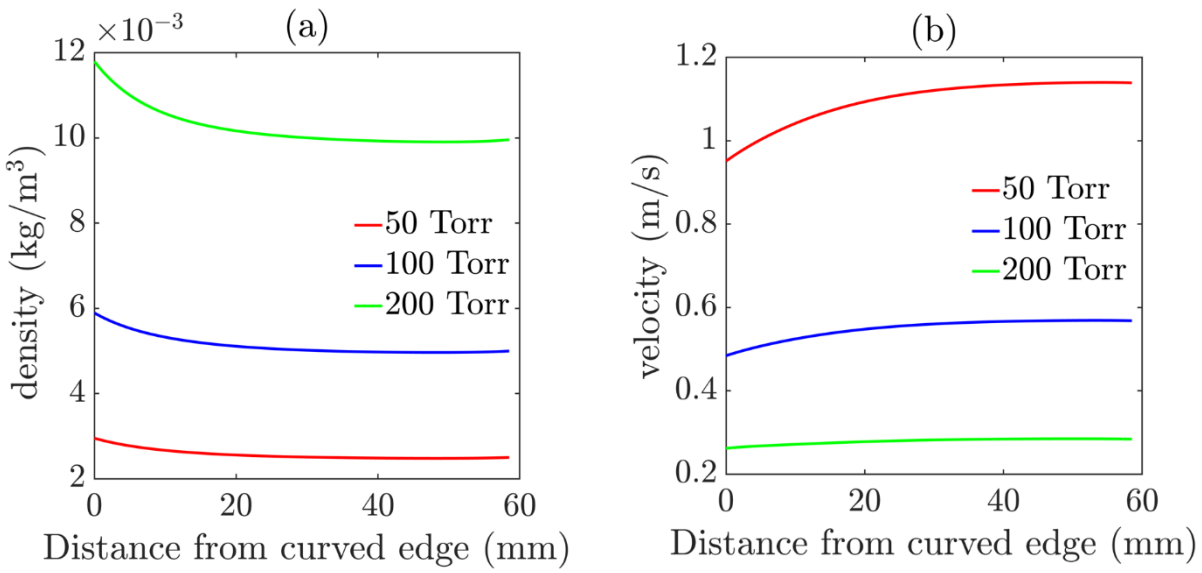

Figure 1.9 (a) Density of mixture in the free-stream region over the heated graphite plate (b) Streamwise velocity in the free-stream region over the heated graphite plate

The effects of increasing pressure discussed above are caused by two underlying physical mechanisms. First, an increase in pressure leads to a linear increase in the mixture density due to the ideal gas law, given that the temperature and mixture molecular weight remain nearly constant. As shown in Fig. 1.9(a), the mixture density is quadrupled as the pressure is increased from 50 to 200 Torr. Consequently, the concentration of all species increases proportionally, which in turn increases the rates of reactions following the law of mass action. The result is an increased concentration yield of $W(SeH)_2Se_2$, observed in Fig. 1.7 and 1.8. Second, increasing the pressure causes a decrease in the streamwise velocity due to the law of mass conservation, since injection flow rates are held constant while the mixture density increases. As shown in Fig. 1.9(b), the streamwise velocity decreases by a factor of two as pressure is doubled from 50 to 100 Torr, and a further increase to 200 Torr causes an additional decrease by the same factor. This translates into an increase in convective time scales across the MOCVD chamber, leading to a larger residence time of gas-phase chemical species over the growth substrate. To be specific, the residence time decreases from about 1 second at 200 Torr down to less than 0.25 seconds at 50 Torr, as expected. Consequently, the formation of stable molecules such as $W(SeH)_2Se_2$ is shifted upstream, and their yield increases. This explains why the distribution of $W(SeH)_2Se_2$ on the plate, shown in Fig. 1.8, transitions from a monotonic increase to a plateauing behavior and finally to a state where a clearly identifiable peak can be observed.

1.4.3 Impact of varying precursor injection method

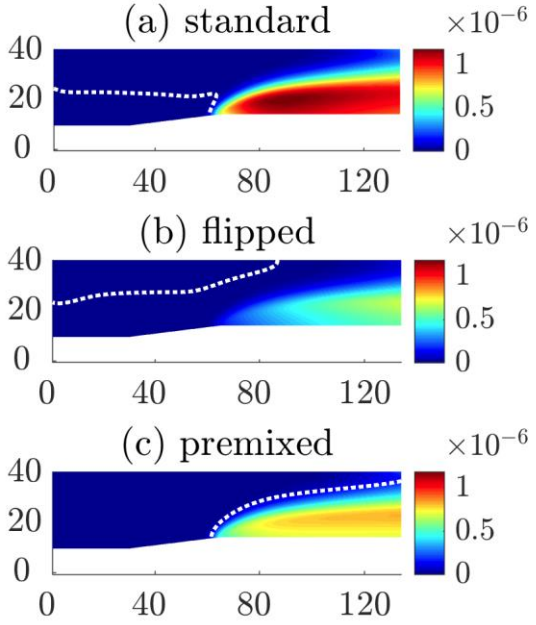

Figure 1.10 (a–c) 2D concentration plots for $W(SeH)_2Se_2$ with the iso-contour of the stoichiometric mixture fraction using different injection methods

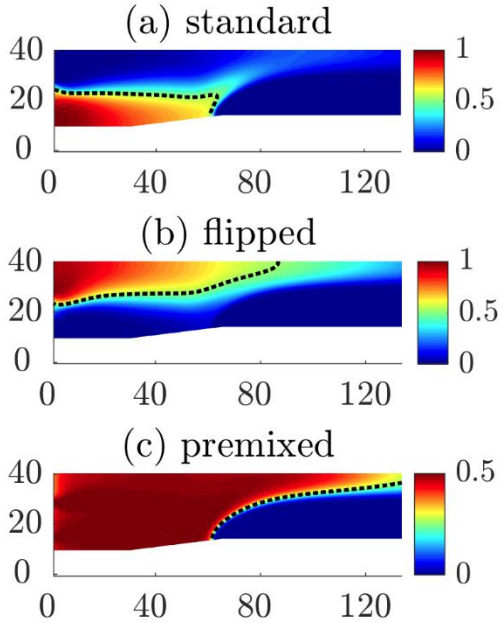

Figure 1.11 (a–c) 2D plots for the mixture fraction with the iso-contour of the stoichiometric mixture fraction using different injection methods

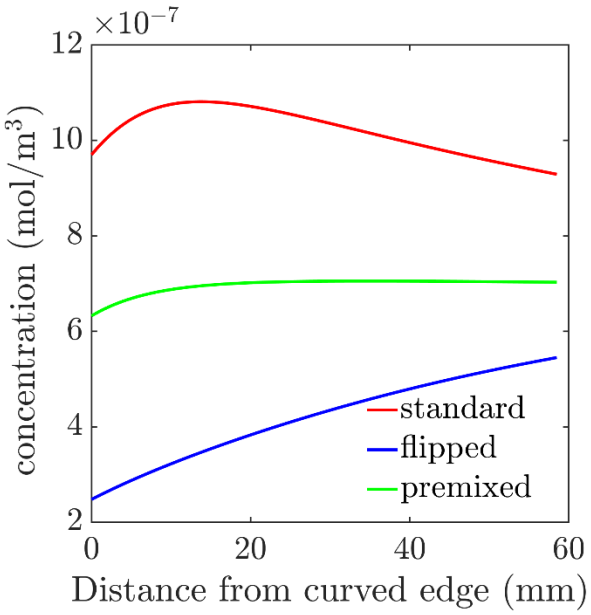

Figure 1.12 Concentration of $W(SeH)_2Se_2$ over the heated graphite plate

Fig. 1.10(a–c) shows the spatial distribution of $W(SeH)_2Se_2$ for three different methods of injecting the two gas-phase precursors (cases A3 and C1–2 in Table 1). The resulting concentration yield of $W(SeH)_2Se_2$ is maximum for the standard injection method, and minimum for flipped injection. However, the vertical spread of this species concentration is the same across all cases since its formation is temperature-driven. The spatial distribution of $W(SeH)_2Se_2$ in the case of standard injection has a peak near the curved edge and shows a decrease thereafter, with significant growth on the plate. For flipped injection, the concentration increases moving downstream, and is higher in the middle of the chamber, which is not advantageous since growth is needed on the plate. When premixed injection is used, the distribution shows a slight increase moving downstream, and relatively higher growth on the plate than the flipped injection case.

Changing the injection methods primarily affects the mixing of the two gas-phase precursors, which in turn impacts the rates of reactions and their location in the chamber. To quantify the effectiveness of mixing, we introduce the mixture fraction Z which is a standard metric used in the study of combustion systems for quantification of fuel and oxidizer mixing levels [40]. The mixture fraction Z is defined as,

$$Z = \frac{\frac{Y_{PC1}}{Y_{PC1,1}}}{\frac{Y_{PC1}}{Y_{PC1,1}} + \frac{Y_{PC2}}{Y_{PC2,2}}} \qquad (1)$$

In the above expression, Y_{PC1} and Y_{PC2} are the local mass fractions of the transition metal precursor $W(CO)_6$ (PC1) and the chalcogen precursor H_2Se (PC2), while $Y_{PC1,1}$ and $Y_{PC2,2}$ are the values of the mass fractions of precursors at their respective injector exit. The mixture fraction is thus a measure of the local transition metal-to-chalcogen precursor ratio at any given point in the MOCVD chamber. It is defined such that $Z = 0$ in the chalcogen precursor stream and $Z = 1$ in

the transition metal precursor stream, varying continuously between these limits. For premixed injection however, $Z = 0.5$ in both the injector streams. The distribution of the mixture fraction in the chamber is shown in Fig. 1.11(a–c) for all injection methods. The stoichiometric mixture fraction Z_{st} is defined as the above equation evaluated at a location where the molar ratio of H_2Se to $W(CO)_6$ is 4:1, which is required for the product $W(SeH)_2Se_2$ to be formed. The value of Z_{st} is 0.52 (0.26 for premixed injection), and its iso-contour is shown on Figs. 1.10 and 1.11(a–c) for all injection methods. For both standard and flipped injection cases, the iso-contour originates in the middle of the chamber. This is not the case when the injection is premixed, as expected.

In the standard injection method, mixing occurs close to the heated region, as shown in Fig. 1.10(a) where the iso-contour of the stoichiometric mixture fraction intersects about 5 mm from the leading edge of the graphite block. This is because the chalcogen jet at the top is heavier due to a much higher concentration than the transition metal jet, thus descending as it moves downstream because of buoyancy effects. The effect of buoyancy can be quantified by computing the Richardson number at each flow injector and taking the ratio of the two scalars (for a comparison of the two jets). In this case, the ratio is about 27 to 1 in favor the PC2 jet. However, the mixing level of both precursors gets leaner towards the heated plate as shown in Fig. 1.10(a) since it is to the right of the stoichiometric mixture fraction iso-contour. This suggests a trade-off between mixing levels and temperature since the mixture is leaner in regions where the temperature is highest. On the contrary, mixing levels improve away from the heated plate where temperature is now lower, resulting in a balance where the formation of $W(SeH)_2Se_2$ is a maximum at a certain height above the plate. Ideally, regions of feasible mixing and high temperature should overlap for maximum yield of the product. The standard injection is closest to this potential since the PC1 jet is closer to the heated plate, allowing for a reasonable balance between mixing levels and high temperature. As a result, species growth on the plate is significant and a clearly identifiable peak is observed in Fig. 1.12.

When the injectors are flipped, the mixture levels are much leaner near the heated region as shown in Fig. 1.10(b), where the iso-contour of the stoichiometric mixture fraction is in the upper half of the chamber. Hence, the trade-off between feasible mixing levels and high temperature is more pronounced relative to the standard injection method. This is because the heavier PC2 jet is at the bottom, and the lighter PC1 jet stays mostly near the top of the chamber due to buoyancy effects. In this case, the ratio of the Richardson numbers is about 2 to 1 in favor the PC2 jet. Thus, mixing occurs above the middle of the chamber, where temperature is about 200 K less than what is required to decompose PC1, which is the rate-limiting species, hence impeding growth. More quantitively, the yield of $W(SeH)_2Se_2$ on the plate is lower by about a factor of three compared to the standard injection, as shown in Fig. 1.12. Additionally, a monotonically increasing trend for the distribution of $W(SeH)_2Se_2$ concentration on the graphite plate can also be observed in Fig. 1.12. This is because the PC1 is transported farther downstream before it decomposes to kickstart formation of products, as shown by the contours of the mixture fraction in Fig. 1.11(b).

In the case of premixed injection, species formation is entirely temperature-controlled, and mixing plays no role, as indicated by the mixture fraction distributed uniformly in Fig. 1.10(c). Premixing the two precursors causes a reduction in the local concentration of the rate-limiting species (PC1) on the heated plate in contrast with the standard injection method. The reduction in concentration of PC1 leads to a decrease in yield of $W(SeH)_2Se_2$ by almost a factor of two as shown in Fig. 1.12,

since the concentration of PC1 is halved locally. Fig. 1.12 also shows that the growth of $W(SeH)_2Se_2$ is more uniform relative to the standard case since decomposition and H_2Se addition reactions happen simultaneously in the region above the heated graphite plate.

1.4.4 Impact of varying H_2Se gas-phase precursor flow rate

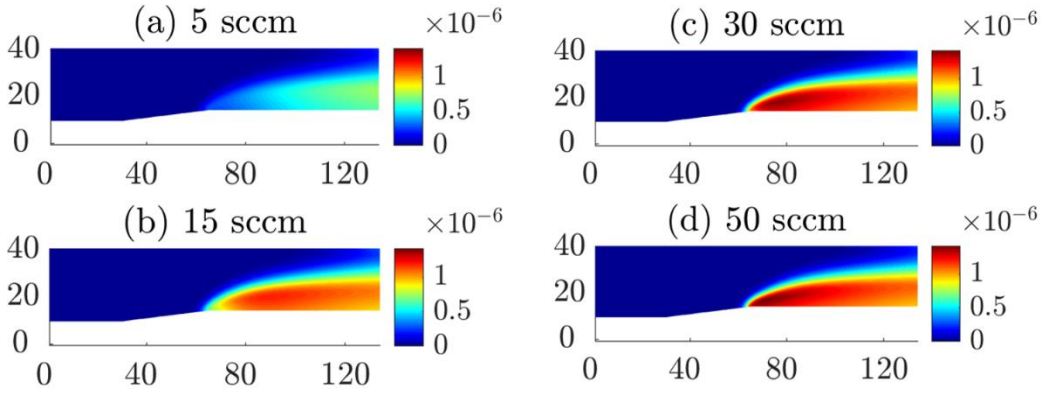

Figure 1.13 (a–d) 2D concentration plots for $W(SeH)_2Se_2$ at different flow rates of H_2Se

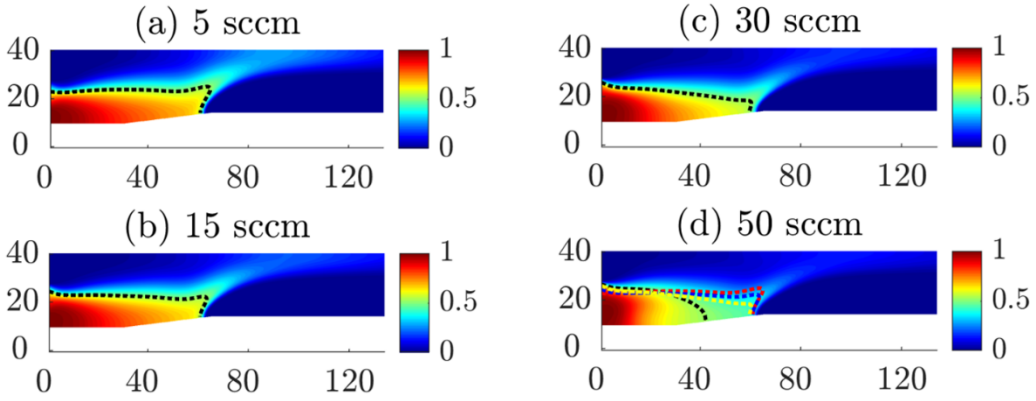

Figure 1.14 (a–d) 2D plots for the mixture fraction with the iso-contour of the stoichiometric mixture fraction at different flow rates of H_2Se

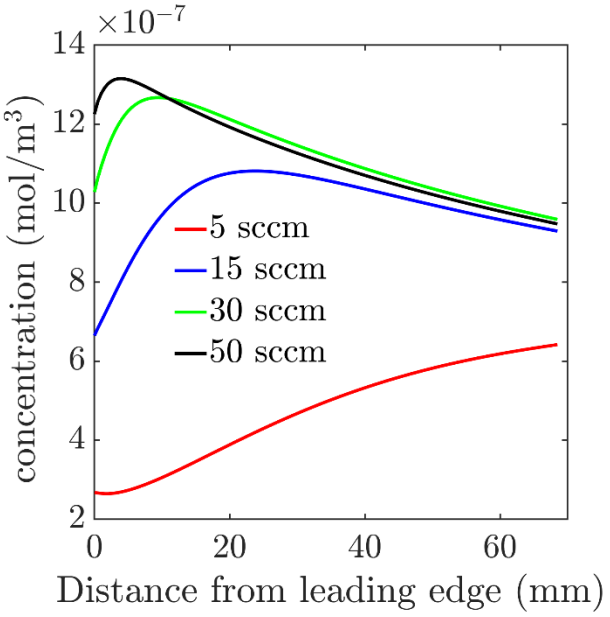

Figure 1.15 Concentration of $W(SeH)_2Se_2$ over the heated graphite plate

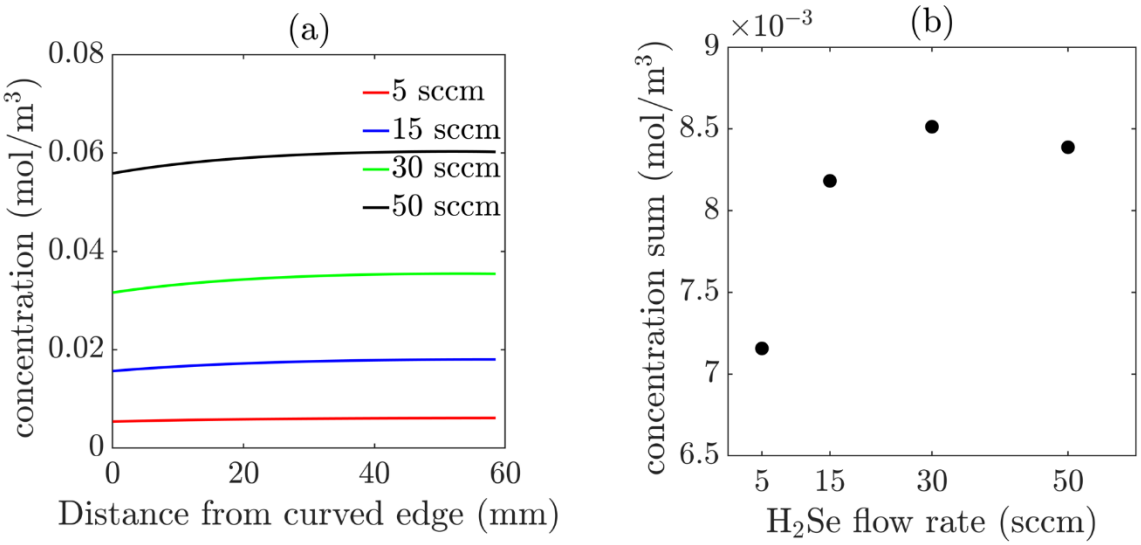

Figure 1.16 (a) Concentration of H_2Se over the heated graphite plate (b) Sum of concentration of all tungsten species sans $W(CO)_{4–6}$ in the heated region over the graphite plate

Fig. 1.13(a–d) shows the spatial distribution of $W(SeH)_2Se_2$ concentration for cases D1–3 and A3 (Table 1), ranging from 5–50 sccm of flow rates for the chalcogen (H_2Se) gas-phase precursor. As explained in the other sections, the vertical spread of this species concentration is the same across all cases since its formation is temperature-controlled. The concentration yield of $W(SeH)_2Se_2$ increases moving downstream at the lowest tested flow rate of 5 sccm and shows an increase towards the leading edge of the graphite block as the H_2Se flow rate is increased. The magnitude

of the concentration yield also increases with an increasing flow rate, however, there is no significant increase in yield when going from 30 to 50 sccm. These observations are emphasized in Fig. 1.15, which shows a monotonically increasing trend for $W(SeH)_2Se_2$ concentration at the lowest flow rate of the chalcogen precursor, and a clearly identifiable peak for the rest, moving upstream as the flow rate is increased. The yield is almost doubled when the flow rate is increased from 5 to 15 sccm, with an additional 10% increase observed for a flow rate of 30 sccm. Moving from 30 to 50 sccm shows no significant increase in yield, as stated earlier.

Increasing the flow rate of H_2Se affects its concentration and mixing with the transitional metal precursor. Fig. 1.16(a) quantifies the effect of increasing the chalcogen precursor flow rates on its concentration, showing an almost linear increase. As a result of increased H_2Se concentration, the yield of $W(SeH)_2Se_2$ shows an increase with increasing flow rates, as observed in Fig. 1.15. This is because the formation of $W(SeH)_2Se_2$ requires a molar ratio of chalcogen to transition metal precursor to be 4:1, thus the additional H_2Se in the domain causes rates of product formation to increase. Additionally, H_2Se addition reactions can occur earlier in the domain as the concentration of H_2Se increases, thus the product $W(SeH)_2Se_2$ can form earlier as well. This is observed in Fig. 1.15 which shows the peak of $W(SeH)_2Se_2$ distribution on the graphite plate moving upstream with an increasing flow rate of H_2Se.

The effect of increasing the chalcogen precursor flow rate on mixing is shown in Fig. 1.14(a–d), wherein each sub-figure shows the iso-contour of the mixture fraction in black. Fig. 1.14(d) however, shows all four stoichiometric mixture fraction iso-contours (red/blue/yellow/black, in that order for increasing H_2Se). In the first two cases (5 and 15 sccm of H_2Se, respectively), no significant difference in mixing levels can be observed in Fig. 1.14(d), wherein the red and the blue contours are coincident. These observations can be linked with Fig. 1.16(b), which plots the sum of the concentration all tungsten species above the plate in the region with a temperature of 800 K or higher. Moving from 5 to 15 sccm of chalcogen precursor, the concentration of tungsten species increases considerably, as also observed in the line plot for $W(SeH)_2Se_2$ in Fig. 1.15. However, as the flow rate of H_2Se is increased to 30 sccm, the mixing of the transition metal and chalcogen precursor is affected slightly, with the yellow contour in Fig. 1.14(d) moving slightly upfront. Concurrently, the increase in tungsten species concentration is not significant as observed by the significantly lesser upward movement of the dot in Fig. 1.16(b) when moving from 15 to 30 sccm of chalcogen precursor flow rate. Finally, at 50 sccm of H_2Se, the mixing of the two precursors is affected most significantly, as shown in Fig. 1.13(d) with the location of the black contour being farthest upstream relative to the other three iso-contours. This considerable movement upstream indicates that mixing occurs very early in the domain, hence there is a higher deficiency of the transition metal precursor in the heated region relative to the case with a flow rate of 30 sccm of H_2Se. Consequently, a decrease in the concentration sum of tungsten species is observed in Fig. 1.16(b). As highlighted before, this observation can be linked with Fig. 1.15, which also shows a decrease in the concentration yield of $W(SeH)_2Se_2$.

1.4.5 Discussion

Based on the results and analysis presented in the previous four subsections (1.4.1–4), a few recommendations can be made for optimum growth conditions of WSe_2. These follow the same order in which results were presented. Starting with growth temperature, it has been reported in literature [25,26] that an increase in growth temperature results in a decrease in nucleation density. This matches with the results obtained from our CFD simulations, where the concentration of $W(SeH)_2Se_2$ decreases atop the graphite plate with an increase in temperature. Further investigation, however, is required since the current model does not incorporate surface chemical kinetics. The growth of WSe_2 is also highly dependent on chamber pressure, and our results indicate that a higher chamber pressure is conducive to growth. However, we cannot make a definitive statement since increasing the pressure beyond our tested range may have a negative effect on WSe_2 growth. Furthermore, given the current MOCVD geometry, the standard injection method gives the best yield among all three injection techniques that were tested. Finally, a higher H_2Se flow rate is in general better (given a fixed $W(CO)_6$ flow rate). However, the increase in flow rates of the chalcogen precursor (H_2Se) is not beneficial beyond a flow rate of 30 sccm.

1.5. Conclusion

In this chapter, the synthesis of WSe_2 from $W(CO)_6$ and H_2Se gas-phase precursors in an MOCVD reactor used by researchers at the Penn State 2D Crystal Consortium (2DCC) facility is investigated numerically using Computational Fluid Dynamics (CFD). The numerical model incorporates heat transfer and fluid mechanics with a detailed gas-phase chemical kinetics mechanism grounded in fundamental principles, presented in a previous study by the authors. The focus of this work was to use CFD as an analysis tool to study the effect of varying reactor operating conditions on WSe_2 crystal growth. This was achieved by varying four process parameters independently of each other (growth temperature, chamber pressure, precursor injection method and H_2Se gas-phase precursor flow rate) and observing the impact on $W(SeH)_2Se_2$ concentration yield and its distribution on the growth substrate. This species was chosen since it represents the thermodynamic endpoint in the chemical model, analogous to WSe_2 in the experiments. The following conclusions can be argued based on our analysis. Firstly, increasing the growth temperature impedes the concentration yield of $W(SeH)_2Se_2$, due to a shift in chemical equilibrium moving away from its formation. Second, an increase in chamber pressure is conducive to growth of $W(SeH)_2Se_2$, thanks to higher concentration of reactants and a decrease in convective transport. Third, the standard injection method for injecting the gas-phase precursors is most effective for maximizing $W(SeH)_2Se_2$ yield, since it aids decomposition of the transition metal precursor. Finally, increasing the chalcogen precursor (H_2Se) flow rate is beneficial for higher yield of $W(SeH)_2Se_2$, however, it offers diminishing returns above a flow rate of 30 sccm.

Chapter 2.

Comparison of W/Se and Mo/Se chemical mechanisms

2.1 Introduction

Molybdenum diselenide ($MoSe_2$) is another member of the TMD family that is analogous to WSe_2. Since $MoSe_2$ is not the focus of this thesis, we will not discuss properties make this material stand apart from its counterparts. There is extensive literature, however, that focuses on studying its properties and especially its growth kinetics using Chemical Vapor Deposition (CVD). In this context and having utilized CFD to study the growth kinetics of WSe_2 as seen in Chapter 1, it was deemed worthwhile to extend this framework to the study of $MoSe_2$.

The focal point of this chapter is to do a qualitative comparison of the W/Se chemical mechanism with the Mo/Se chemical mechanism, the latter also developed using the approach explained in [33]. However, it is important to note that both mechanisms have the end-point species as XSe_3 instead of $X(SeH)_2Se_2$ where X is the transition metal atom. Additionally, both mechanisms incorporate W/Mo as a species (to be precise, a transition metal atom). As a result, both mechanisms have a total of 59 species, instead of the 57 species mechanism used for CFD simulations in Chapter 1. As a result of these changes, two sets of analysis can be carried out: **(a)** a comparison between the W/Se mechanism in Chapter 1 and Chapter 2; and **(b)** a comparison between W/Se and Mo/Se mechanisms (both having the same set of species).

One could in theory do the first comparison (which was done during this research), but it was decided to only present the findings for comparison **(b).** This is simply because the chemical kinetics model is for the gas-phase, and CFD simulations of the 'new' W/Se mechanism show that the yield of WSe_2 improves significantly over the heated graphite plate. However, we are interested in the yield of WSe_3 in the new W/Se mechanism, thus the focal point is comparison **(b)**. It is crucial to note that if surface reactions are incorporated into the chemical kinetics model, WSe_2 would be a Quantity of Interest (QOI) as well, thus comparison **(a)** would become relevant to this discussion.

For consistency, the CFD simulations for both the W/Se and the Mo/Se mechanisms were run at the baseline test conditions outlined in Section 2.2 of Chapter 1 (1.2.2). Since W and Mo have different atomic weights, the mass fraction of $W(CO)_6$ fed to the solver as an input condition differs from that of $Mo(CO)_6$ given the same injector flow rate of 5.4×10^{-4} sccm. The same computational domain was utilized for both simulations, as described in Section 1.3.3. What follows in this chapter is an analysis of both mechanisms using the concentration yield of $W/MoSe_3$ as the QOI, which is achieved using Reaction Pathway Analysis and developing a Reaction Graph for both mechanisms.

2.2 Analysis and Comparison

To analyze a given set of chemical reactions, and highlight the major reactions and species, it is useful to perform a Reaction Pathway Analysis (RPA). As the name suggests, this method is helpful in delineating the major pathways in a chemical mechanism, usually from the reactant or some early species all the way down to a final product or products. Before proceeding onto the analysis, it is helpful to present a brief introduction to this technique.

It is known that reactive CFD involves the numerical solution of $N-1$ species equations, where N is the number of species in the chemical kinetics mechanism. For RPA, the **volumetric** source term (denoted by $\dot{\boldsymbol{\omega}}_{\boldsymbol{vol}}$) is computed for each reaction involving the species under consideration. As an example, consider the following set of reactions involving species A:

$$A \rightarrow B + C \qquad (1)$$
$$A + D \leftrightarrow E \qquad (2)$$
$$F + G \rightarrow A \qquad (3)$$

From the above set of reactions, we can infer that the first reaction *consumes* A, thus $\dot{\boldsymbol{\omega}}_{\boldsymbol{vol}}$ would be a negative number. The second reaction is a two-way reaction, thus $\dot{\boldsymbol{\omega}}$ is computed as the difference of the two rates of reaction. Given that this difference is computed as $\dot{\boldsymbol{\omega}}_{\boldsymbol{prod}} - \dot{\boldsymbol{\omega}}_{\boldsymbol{cons}}$, a positive scalar in this case would mean that species A is being produced from reaction 2 when the overall path is considered. The third reaction is where species A is *produced*, thus $\dot{\boldsymbol{\omega}}$ would be a positive number in this case. These three scalars can be tabulated, and comparing their magnitudes is indicative of the major pathway(s) of both production and consumption. This allows us to infer which species to consider next for RPA, and this process is continued until there is a clear pathway(s) from the reactant(s) to the product(s).

The mathematical formulation of RPA (i.e. computation of the volumetric source term) is

$$\dot{\boldsymbol{\omega}}_{\boldsymbol{vol}} = \int \dot{\boldsymbol{\omega}}\, \boldsymbol{dV} \qquad (1)$$

where $\dot{\boldsymbol{\omega}}$ is computed using the rate law, which in turn requires knowing the temperature T and the activation energy E_a for the reaction being considered. The volumetric integration is carried out numerically as one would expect. It is important to note, however, that the domain under consideration does not have to be the entire computational domain since reactions occur in a limited region above the heated plate. Additionally, RPA is only carried out for selected species in the mechanism, that are considered *major* (quantified by their concentration yield).

In the above context, it is helpful to recall that in Section 4.1 of Chapter 1 (1.4.1), we presented the Reaction Graph for the W/Se chemical mechanism which delineates the pathway from the earliest species to the final product species. A modified Reaction Graph for the W/Se mechanism is presented in Fig. 2.1 below, showing WSe_3 as the final product. Comparing Fig. 2.1 below with Fig 1.3 (Chapter 1) shows that the major difference between the two mechanisms is the formation of the species WSe_3. More importantly, there is only one type of reaction that can form WSe_3 i.e. the loss of H_2Se from $W(SeH)_2Se_2$. Therefore, the species $W(SeH)_2Se_2$ is no longer considered

major in the new W/Se mechanism, which is the second difference from the old model. This is because the $W(SeH)_2Se_2$ that is formed decomposes into WSe_3 in the heated region above the plate. In short, the pathway to form WSe_3 is simply an extrapolation on the older W/Se mechanism that does not contain this species.

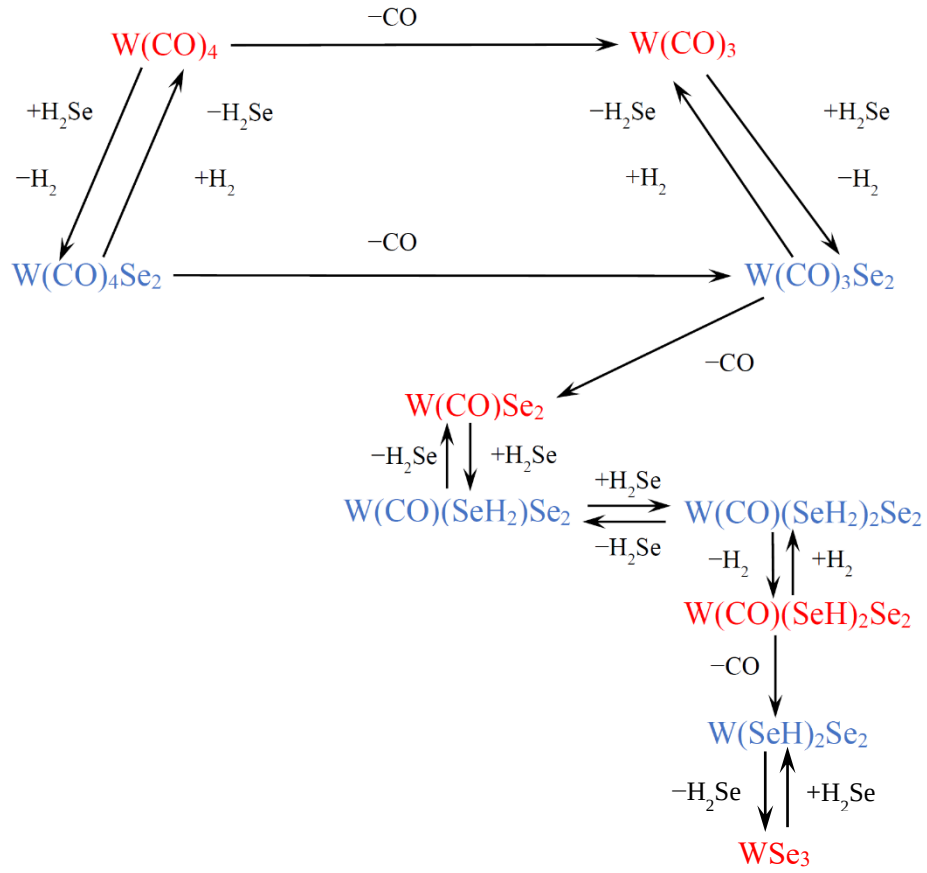

Figure 2.1 Reaction Graph for the W/Se mechanism showing major species in red

On the contrary, analyzing the Mo/Se mechanism using RPA yields interesting differences in how $MoSe_3$ is produced when compared with WSe_3. A Reaction Graph was also constructed for the Mo/Se mechanism and is shown in Fig. 2.2. It is interesting to observe from the figure that the Reaction Graph for the Mo/Se chemical model is like its W/Se counterpart up to the species $Mo(CO)Se_2$. To be precise, the pathways from the earlier species to $Mo(CO)Se_2$ and the major species involving them are the same as found in the W/Se model. Thereafter, however, we find two crucial differences in the pathway from $Mo(CO)Se_2$ to the product $MoSe_3$.

First, $MoSe_2$ is a major species in the model as opposed to WSe_2. This is because the activation energy E_a for the reaction that forms $MoSe_2$ via a decomposition reaction is much lower than the reaction found in the W/Se mechanism (206 vs 276 kJ/mol), with an Arrhenius pre-exponential factor on the same order of magnitude. However, it must be noted that the major consumption pathway for $Mo(CO)Se_2$ is the H_2Se addition/loss reaction that forms $Mo(CO)(SeH_2)Se_2$. On the contrary, the major production pathway for $MoSe_2$ is the decomposition of $Mo(CO)Se_2$ – an important nuance.

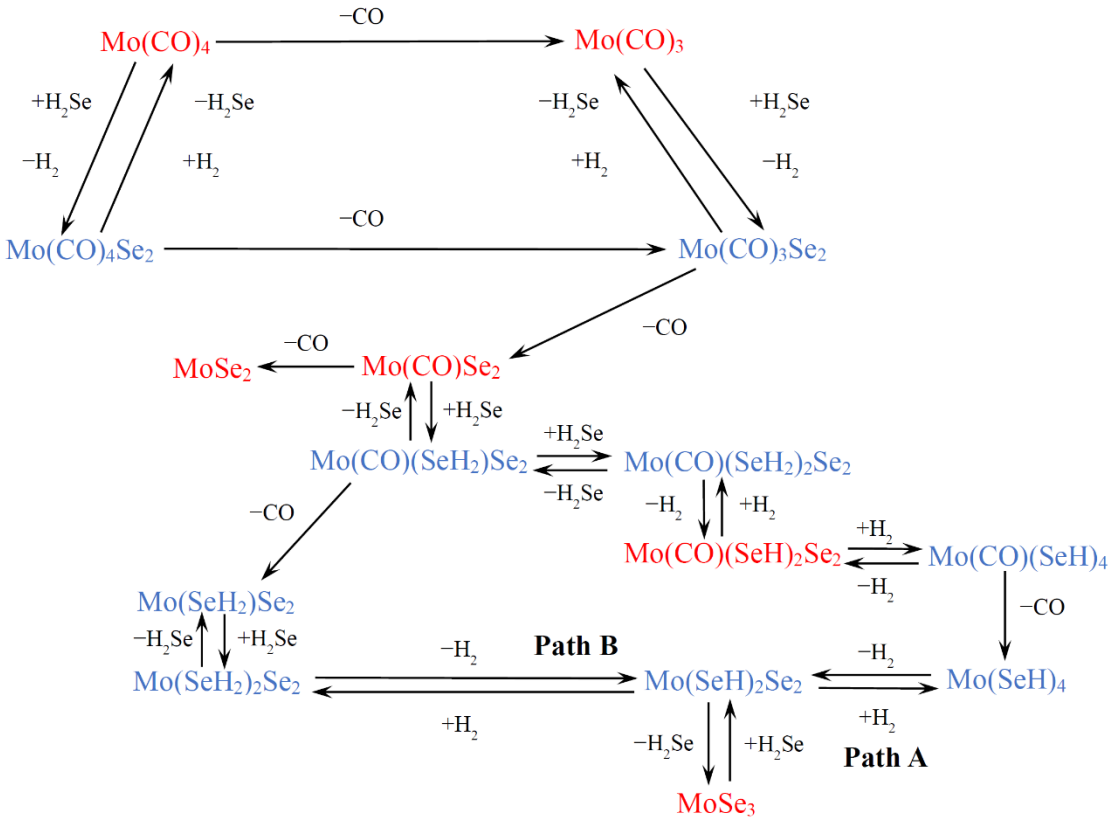

Figure 2.2 Reaction Graph for the Mo/Se mechanism showing major species in red

Second, $Mo(CO)(SeH)_2Se_2$ does not have a **direct** pathway to the penultimate species in the Reaction Graph i.e. $Mo(SeH)_2Se_2$. This is despite having a decomposition reaction for $Mo(CO)(SeH)_2Se_2$ in the chemical mechanism that forms $Mo(SeH)_2Se_2$. However, the activation energy E_a for this reaction is about 340 kJ/mol, and the plate temperature of 850°C is not sufficient for it to occur. As a result, production of $Mo(SeH)_2Se_2$ occurs via two alternative pathways (labeled *A* and *B*), shown in Fig. 2.2. However, four of these six reactions are two-way, which means that the intermediate species has two options – go back to the reactant or proceed forward to form the next species. This affects the yield of $MoSe_3$ that can be obtained when compared with the possibility of these reactions being one-way, since $MoSe_3$ is formed via decomposition of $Mo(SeH)_2Se_2$.

The two pathways that form the species $Mo(SeH)_2Se_2$ do not contribute equally, however. Calculations done using RPA suggest that 70% of the production of this species comes from the pathway *A* involving the loss of H_2 from $Mo(SeH)_4$. This is expected, since $Mo(SeH)_4$ is an intermediate species in this path that stems from $Mo(CO)(SeH)_2Se_2$, which as discussed earlier, cannot decompose directly to produce $Mo(SeH)_2Se_2$. However, pathway *A* is not significantly dominant over pathway *B*, which is generally considered to be the case when one pathway contributes 90% or more of the total production or consumption of a species. This is because the decomposition of $Mo(SeH_2)_2Se_2$ to form $Mo(SeH)_2Se_2$ in pathway *B* is essentially a one-way

reaction, since the backward reaction has an activation energy E_a of about 394 kJ/mol, and an Arrhenius pre-exponential factor that is an order of magnitude less than the forward reaction (for which E_a is 72 kJ/mol).

2.3 Conclusion

In this chapter, we focused on analyzing two analogous chemical mechanisms involving two TMDs: W/Se and Mo/Se. These mechanisms are the chemical kinetics model fed to the reactive CFD solver (NGA) to simulate the growth of the TMDs in an MOCVD chamber. Post-processing of the CFD results coupled with RPA can be utilized to construct Reaction Graphs for both chemical mechanisms. With the aid of the Reaction Graph for both mechanisms, we were able to demonstrate similarities and differences in the pathways that lead from the earlier species in the model to the final product (designated QOI). These results can be used to conduct numerical experiments in helping experimental researchers finding optimal operating parameters to increase the yield of $MoSe_3$. Given the differences in the yield of WSe_3 and $MoSe_3$, it is reasonable to conclude that a higher plate temperature is required to achieve an increased yield for $MoSe_3$. Furthermore, we know that this higher plate temperature would likely produce a similar yield as obtained for WSe_3 at the current plate temperature (850°C). The alternative method to increase the yield of $MoSe_3$ is to increase the flow rate of $Mo(CO)_6$ at the injector, since different atomic weights for W and Mo translate into a different input mass fraction given the same injection flow rate.

Chapter 3.

Analyzing the effect of chamber geometry on WSe_2 growth

3.1 Introduction

In Chapter 1, we explored the variation in the MOCVD chamber operating conditions using reactive CFD. These numerical experiments, as one would call them, assumed that the chamber/reactor geometry is fixed. This is taken to mean that its key dimensions as well as the features inside of it such as the location of the heated plate, the slope of the quartz ramp and the position of the injectors are a replica of the actual (physical) model used by experimental researchers. However, we can harness the power of CFD simulations to explore the effect of varying chamber geometry itself on the growth of WSe_2.

The use of CFD as a tool for this task is an even more attractive option simply because varying the geometry would require another physical copy with the new dimensions, which is more expensive than simply changing injector flow rates in an experiment. Multiple numerical experiments can be performed, and the changes made to the geometry can either be subtle or significant, as required. In this context, the current chamber geometry was modified by displacing the graphite block and by association, the heated plate towards and away from the flow injectors by 5 mm (i.e. upstream and downstream). This gives us two new chamber configurations to use in reactive CFD simulations, as shown in Fig. 3.1 below.

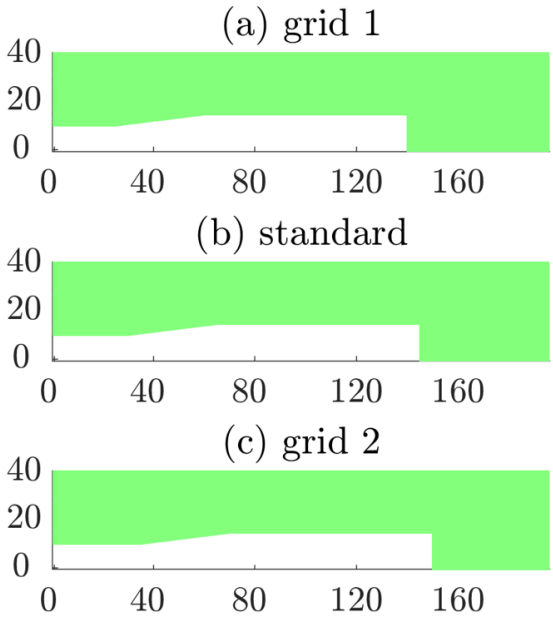

Figure 3.1 Standard and modified MOCVD chamber geometries (wall cells in white)

For consistency, no other chamber geometry feature was modified, and the spatial resolution of the grid was kept constant as well. The distance of the heated plate from the flow injectors is thus another process parameter which can be varied to study its effect on WSe_2 growth. This feature

was chosen because it affects the magnitude of the mass fraction of the transition metal precursor $W(CO)_6$ (PC1) in the heated region. Consequently, the production of $W(SeH)_2Se_2$ is influenced, since the decomposition of PC1 required to kickstart formation of intermediate products is a temperature-controlled reaction. Considering what is known (from Chapter 1) about mixing levels of the two gas-phase precursors and plate temperature affecting WSe_2 growth, it is worthwhile to experiment with the location of the heated plate in the chamber.

Before proceeding to a discussion on the results, it is important to note that the chemical kinetics mechanism used for the reactive CFD simulations in this chapter is the same as used in Chapter 1 (see 1.3.1). This was done to ensure consistency with the numerical experiments used to study the effects of varying process parameters, and because we have good insight into the flow physics and growth kinetics of this problem. Additionally, the values of the process parameters used for these runs (see Chapter 1) correspond with case **A3** in Table 1.

3.2 Results and Discussion

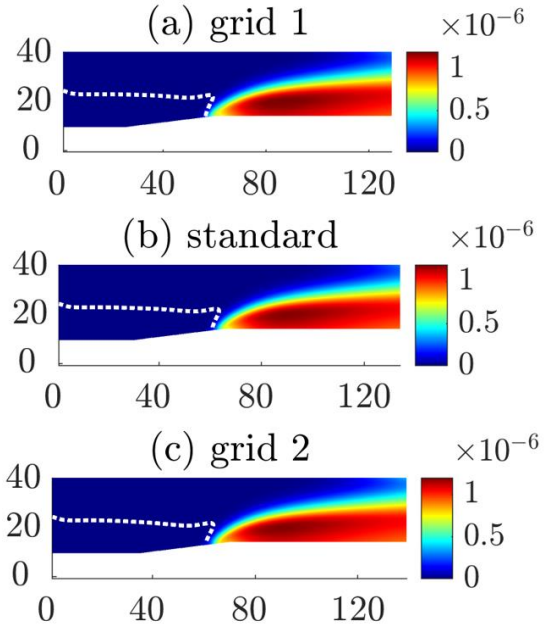

Figure 3.2 (a–c) 2D concentration plots for $W(SeH)_2Se_2$ for different chamber geometries with the iso-contour of the stoichiometric mixture fraction

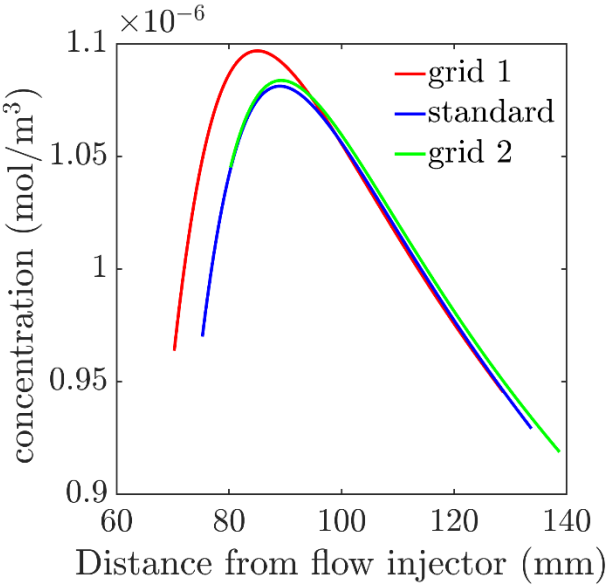

Figure 3.3 Concentration of $W(SeH)_2Se_2$ over the heated graphite plate

Fig. 3.2(a–c) shows the spatial distribution of $W(SeH)_2Se_2$ for all three chamber geometries. No significant differences in distribution, both horizontally and vertically, can be observed by looking at these plots. The inception point does not seem to have displaced either, except the fact that its distance from the bottom injector changes with each grid configuration. This is expected since all process parameters were kept constant across all three configurations. For clarity, the line plots of concentration yield of $W(SeH)_2Se_2$ over the heated plate for all three configurations are shown in Fig. 3.3.

As can be seen in Fig. 3.3, the concentration yield of $W(SeH)_2Se_2$ is the highest for grid 1, wherein the heated plate has been displaced 5 mm upstream. The peak of the species distribution shifts upstream as well, but that is simply because of the displacement of the heated plate. As the graphite block and the heated plate are displaced downstream, the yield shows a decrease. Overall, the decrease in the yield of $W(SeH)_2Se_2$ is found to be monotonic. However, this is not clear from the figure, since the concentration yield of $W(SeH)_2Se_2$ is slightly higher for the configuration labeled grid 2, downstream of the peak of the distribution curve.

The increase in the concentration yield of when the graphite block (and plate) is displaced upstream is explained with the aid of Fig. 3.2, which has the iso-contour of the stoichiometric mixture fraction Z_{st} juxtaposed on the 2D plot of $W(SeH)_2Se_2$ concentration in the chamber. In the case of grid 1, the heated region is now closer to the iso-contour of Z_{st}, thus more of PC1 is available for decomposition. As expected, this results in the highest concentration yield of $W(SeH)_2Se_2$ among all three configurations tested. The monotonic decrease in the yield of this species is also consistent with the expected trend, since displacing the heated plate downstream means that the local mass fraction of PC1 in the heated region deteriorates, resulting in a decreased yield of the final product.

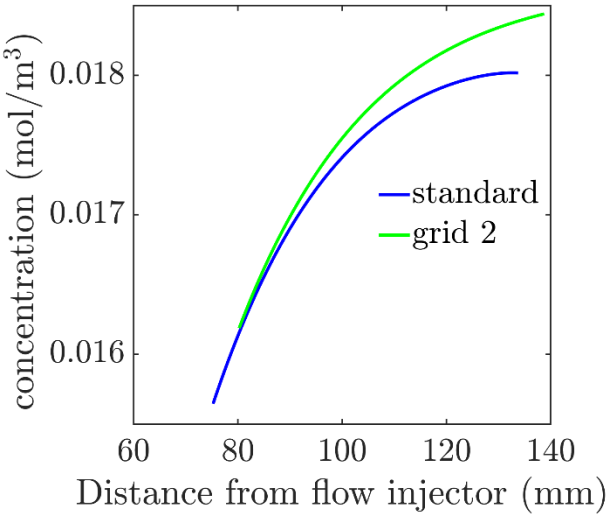

Figure 3.4 Concentration of H_2Se over the heated graphite plate

In the case of grid 2, however, the slightly higher concentration of $W(SeH)_2Se_2$ relative to the standard configuration, highlighted earlier, suggests that there is a compensating factor at work. This is found to be the increased concentration of H_2Se (PC2) above the heated plate in the case of grid 2, as shown in Fig. 3.4. When the graphite block (and thus, the quartz ramp) is displaced downstream, there is an increased flow area available for the gas-phase species to occupy. Since the chalcogen gas-phase precursor (PC2) is heavier than the transition-metal precursor (PC1), more of it can descend towards the heated plate as it moves downstream. Consequently, product formation is facilitated given that H_2Se addition reactions have no energy barrier. Thus, a balance between two competing effects (decreased availability of PC1 and an increase in PC2 concentration) is the cause of the slightly higher curve for grid 2 in Fig. 3.3, with the former effect being slightly dominant.

3.3 Conclusion

This chapter focused on analyzing the effect of chamber geometry on the growth of WSe_2 by studying the impact on the concentration yield of $W(SeH)_2Se_2$. Albeit there are various geometry features that can be modified for this purpose, the (horizontal) distance of the graphite block (and the heated plate) from the flow injectors was selected. This is because we know from the analysis in Chapter 1 that the yield of $W(SeH)_2Se_2$ is dependent on the mixing levels of the two-gas phase precursors and the plate temperature. The mixing level is quantified by computing the local mixture fraction Z, and the overlap of the heated region with a greater magnitude of Z improves yield of $W(SeH)_2Se_2$. By displacing the graphite block upstream and downstream, and analyzing the results from reactive CFD simulations, we conclude that moving the heated plate closer to the flow injectors improved the yield of $W(SeH)_2Se_2$. However, the opposite case did not have a significant decrease in yield of this species since the greater flow area allowed the chalcogen precursor to descend and inhabit the heated region. This mechanism compensates the decreased local mass fraction of PC1 as quantified by the mixture fraction Z.

REFERENCES

[1] K.F. Mak, C. Lee, J. Hone, J. Shan, T.F. Heinz, Atomically Thin MoS_2: A new direct-gap semiconductor, Phys. Rev. Lett. 105 (2010) 136805.

[2] W. Liu, J. Kang, D. Sarkar, Y. Khatami, D. Jena, K. Banerjee, Role of metal contacts in designing high-performance monolayer n-type WSe_2 field effect transistors, Nano Lett. 8 (2013) 1983–1990.

[3] H. Zeng, G.-B. Liu, J. Dai, Y. Yan, B. Zhu, R. He, L. Xie, S. Xu, X. Chen, W. Yao, X. Cui, Optical signature of symmetry variations and spin-valley coupling in atomically thin tungsten dichalcogenides, Sci. Rep. 3 (2013) 1608.

[4] D. Xiao, G.-B. Liu, W. Feng, X. Xu, W. Yao, Coupled spin and valley physics in monolayers of MoS_2 and other group-VI dichalcogenides, Phys. Rev. Lett. 108 (2012) 196802.

[5] W. Choi, N. Choudhary, G.H. Han, J. Park, D. Akinwande, Y.H. Lee, Recent development of two-dimensional transition metal dichalcogenides and their applications, Mat. Tod. 20 (2017) 116–130.

[6] W. Bao, X. Cai, D. Kim, K. Sridhara, M.S. Fuhrer, High mobility ambipolar MoS_2 field-effect transistors: Substrate and dielectric effects, Appl. Phys. Lett. 102 (2013) 042104.

[7] G.L. Frey, S. Elani, M. Homyonfer, Y. Feldman, R. Tenne, Optical-absorption spectra of inorganic fullerenelike MS_2 (M= Mo, W), Phys. Rev. B 57 (1998) 6666–6671.

[8] M.R. Islam, N. Kang, U. Bhanu, H.P. Paudel, M. Erementchouk, L. Tetard, M.N. Leuenberger, S.I. Khondaker, Tuning the electrical property via defect engineering of single layer MoS_2 by oxygen plasma, Nanoscale 6 (2014) 10033–10039.

[9] P. Tonndorf, R. Schmidt, P. Bottger, X. Zhang, J. Borner, A. Liebig, M. Albrecht, C. Kloc, O. Gordan, D.R.T. Zahn, S.M. de Vasconcellos, R. Bratschitsch, Photoluminescence emission and Raman response of monolayer MoS_2, $MoSe_2$, and WSe_2, Opt. Express 21 (2013), 4908–16.

[10] H. Li, Z. Yin, Q. He, H. Li, X. Huang, G. Lu, D.W.H. Fam, A.I.Y. Tok, Q. Zhang, H. Zhang, Fabrication of Single- and Multilayer MoS_2 Film-Based Field-Effect Transistors for Sensing NO at Room Temperature, Small 8 (2012) 63–67.

[11] H. Fang, S. Chuang, T.C. Chang, K. Takei, T. Takahashi, A. Javey, High-Performance Single Layered WSe_2 p-FETs with Chemically Doped Contacts, Nano Lett. 12 (2012) 3788–92.

[12] J.-K. Huang, J. Pu, C.-L. Hsu, M.-H. Chiu, Z.-Y. Juang, Y.-H. Chang, W.-H. Chang, Y. Iwasa, T. Takenobu, L.-J. Li, Large-Area Synthesis of Highly Crystalline WSe_2 Monolayers and Device Applications, ACS Nano 8 (2014) 923–930.

[13] Y.-C. Lian, N. Lu, N. P.-Lopez, J. Li, Z. Lin, X. Peng, C.H. Lee, L. Calderin, P.N. Browning, M.S. Bresnehan, M.J. Kim, T.S. Mayer, M. Terrones, J.A. Robinson, Direct Synthesis of van der Waals Solids, ACS Nano 8 (2014) 3715–3723.

[14] S. Wang, Y. Rong, Y. Fan, M. Pacios, H. Bhaskaran, K. He, J.H. Warner, Shape Evolution of Monolayer MoS_2 Crystals Grown by Chemical Vapor Deposition, Chem. Mater. 26 (2014) 6371–6379.

[15] X. Ling, Y.-H. Lee, Y. Lin, W. Fang, L. Yu, M.S. Dresselhaus, J. Kong, Role of the Seeding Promoter in MoS_2 Growth by Chemical Vapor Deposition, Nano Lett. 14 (2014) 464–472.

[16] G.Z. Magda, J. Peto, G. Dobrik, C. Hwang, L.P. Biro, L. Tapaszto, Exfoliation of large-area transition metal chalcogenide single layers, Sci. Rep. 5 (2015) 14714.

[17] X. Hong, J. Kim, S.-F. Shi, Y. Zhang, C. Jin, Y. Sun, S. Tongay, J. Wu, Y. Zhang, F. Wang, Ultrafast charge transfer in atomically thin MoS_2/WS_2 heterostructures, Nat. Nanotechnol. 9

(2014) 682–686.
[18] Y. Shi, H. Li, L.-J. Li, Recent advances in controlled synthesis of two-dimensional transition metal dichalcogenides *via* vapour deposition techniques, Chem. Soc. Rev. 44 (2015) 2744–2756.
[19] G.R. Bhimanapati et al. Recent Advances in Two-Dimensional Materials beyond Graphene, ACS Nano 9 (2015) 11509–11539.
[20] X. Zhang, F. Zhang, Y. Wang, D.S. Schulman, T. Zhang, A. Bansal, N. Alem, S. Das, V.H. Crespi, M. Terrones, J.M. Redwing, Defect-Controlled Nucleation and Orientation of WSe_2 on hBN: A Route to Single-Crystal Epitaxial Monolayers, ACS Nano 13 (2019) 3341–3352.
[21] S.M. Eichfeld et al. Highly Scalable, Atomically Thin WSe_2 grown *via* Metal–Organic Chemical Vapor Deposition, ACS Nano 9 (2015) 2080–2087.
[22] K. Kang, S. Xie, L. Huang, Y. Han, P.V. Huang, K.F. Mak, C.-J. Kim, D. Muller, J. Park, High-mobility three-atom-thick semiconducting films with wafer-scale homogeneity, Nat. Lett. 520 (2015) 656–660.
[23] B. Liu, M. Fathi, L. Chen, A. Abbas, Y. Ma, C. Zhou, Chemical Vapor Deposition Growth of Monolayer WSe_2 with Tunable Device Characteristics and Growth Mechanism Study, ACS Nano 9 (2015) 6119–6127.
[24] T. Kwak, J. Lee, B. So, U. Choi, O. Nam, Growth behavior of wafer-scale two-dimensional MoS_2 layer growth using metal-organic chemical vapor deposition, J. Crys. Growth 510 (2019) 50–55.
[25] H. Zhou, C. Wang, J.C. Shaw, R. Cheng, Y. Chen, X. Huang, Y. Liu, N.O. Weiss, Z. Lin, Y. Huang, X. Duan, Large Area Growth and Electrical Properties of p-Type WSe_2 Atomic Layers Nano Lett. 15 (2014) 709–713.
[26] Sarah M. Eichfeld, V.O. Colon, Y. Nie, K. Cho, J.A. Robinson, Controlling nucleation of monolayer WSe_2 during metal-organic chemical vapor deposition growth, 2D Mater. 3 (2016) 025015.
[27] B. Mitrovic, A. Gurary, L. Kadinski, On the flow stability in vertical rotating disc MOCVD reactors under a wide range of process parameters, J. Cryst. Growth 287 (2006) 656–663.
[28] Z. Zhang, H. Fang, Q. Yao, H. Yan, Z. Gan, Species transport and chemical reaction in a MOCVD reactor and their influence on the GaN growth uniformity, J. Cryst. Growth 454 (2016) 87–95.
[29] Z. Nami, O. Misman, A. Erbil, G.S. May, Computer simulation study of the MOCVD growth of titanium dioxide films, J. Cryst. Growth 171 (1997) 154–165.
[30] B. Mitrovic, A. Parekh, J. Ramer, V. Merai, E.A. Armour, L. Kadinski, A. Gurary, Reactor design optimization based on 3D modeling of nitrides deposition in MOCVD vertical rotating disc reactors, J. Cryst. Growth 289 (2006) 708–714.
[31] J. Li, J. Wang, J.-d. Cai, Y.-f. Xu, B.-f. Fan, G. Wang, Numerical simulation and analysis of process parameters of GaN-MOCVD reactor, Int. Commun. Heat Mass 91 (2018) 64–76.
[32] J. Li, Y. Lai, Y. Xu, Z. Chen, Y. Pei, G. Wang, Process parameter analysis and parasitic reaction of ZnO grown through MOCVD, Vacuum 157 (2018) 76–82.
[33] Y. Xuan, A. Jain, S. Zafar, R. Lotfi, N. Nayir, Y. Wang, T.H. Choudhury, S. Wright, J. Feraca, L. Rosenbaum, J.M. Redwing, V. Crespi, A.C.T. van Duin, Multi-scale modeling of gas-phase reactions in metal-organic chemical vapor deposition growth of WSe_2, J. Cryst. Growth 527 (2019) 125247.
[34] A.C.T. van Duin, S. Dasgupta, F. Lorant, W.A. Goddard, ReaxFF: A Reactive Force Field for Hydrocarbons, J. Phys. Chem. A 105 (2001) 9396–9409.

[35] B. Peters, Reaction Rate Theory and Rare Events Simulations, Elsevier, Amsterdam, 2017, p. 212.
[36] O. Desjardins, G. Blanquart, G. Balarac, H. Pitsch, High order conservative finite difference scheme for variable density low Mach number turbulent flows, J. Comput. Phys. 227 (2008), 7125–7159.
[37] B. Savard, Y. Xuan, B. Bobbit, G. Blanquart, A computationally-efficient, semi-implicit, iterative method for the time-integration of reacting flows with stiff chemistry, J. Comput. Phys. 295 (2015) 740–769.
[38] Y. Xuan, G. Blanquart, Numerical modeling of sooting tendencies in a laminar co-flow diffusion flame, Combust. Flame 160 (2013) 1657–1666.
[39] Y. Xuan, G. Blanquart, Effects of aromatic chemistry-turbulence interactions on soot formation in a turbulent non-premixed flame, Proc. Combust. Inst. 35 (2015) 1911–1919.
[40] N. Peters, Turbulent Combustion, Cambridge University Press, Cambridge, 2000, p. 173.